

Supporting Information

Experimental

Dispersions were produced by ultra-sonication (UP 100H Ultrasonic Processor, Hielscher, 100% amplitude, continuous cycle) of the bulk *h*-BN powder in either NMP or isopropanol for 2 hrs. During ultra-sonication dispersions were placed in an ice-bath. After ultra-sonication dispersions were left to settle for over two nights. Finally supernatant was carefully decanted and samples were prepared by drop-casting onto Agar holey-carbon/copper grids (500mesh). The samples were baked for 3 hrs at 135 °C to remove volatile impurities.

Bulk hexagonal boron nitride powders were provided by Saint-Gobain Advanced Ceramics Lauf GmbH with the stated chemical purity >98% *h*-BN, <1.5% O₂, >0.5% B₂O₃. NMP anhydrous and isopropanol were purchased from Sigma-Aldrich and used as received.

Conventional TEM and electron diffraction was carried out using JEOL2010 microscope operated at 200 keV.

Imaging was done using JEM-ARM200F STEM operated at 80 keV with a probe current of ~0.2 nA. The probe convergence angle was 22 mrad. The collection half angle for electrons was 45-170 mrad (Figure 1) and 55-170 mrad (Figure 2).

HRTEM images used for focal series exit wave reconstructions were collected using the double aberration corrected JEOL 2200MCO instrument at University of Oxford. The instrument was operated at 80kV with spherical aberration set to C₃=-3μm in order to partially offset residual C₅ aberration effects. Remaining aberrations higher than the 3rd order that could not be corrected in the instrument were removed from the exit wave post- experimentally using a phase plate.

h-BN Time Series

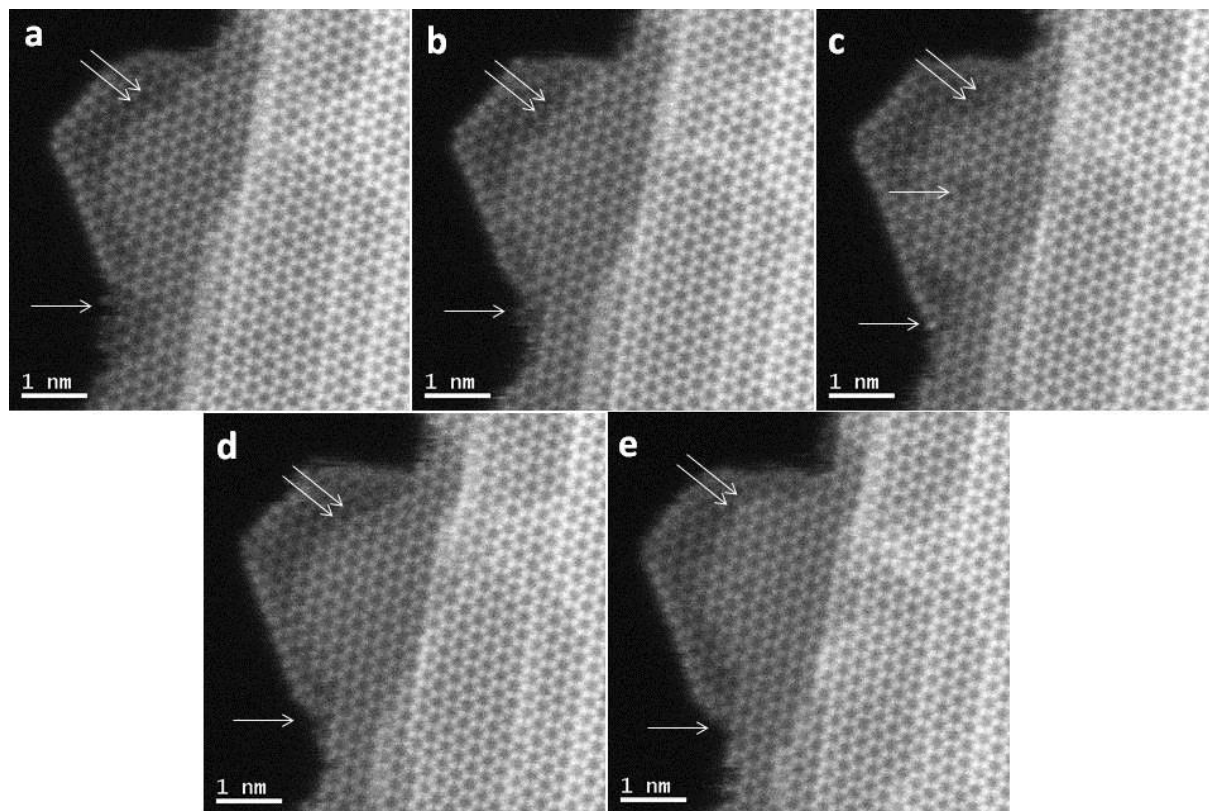


Figure S1. ADF STEM image time series of a *h*-BN nanoflake. Time acquisition per image is 21 seconds. Single and double arrows are used to mark areas where structural changes are observed. The additional arrow in (c) indicates a vacancy site. Time series show the same region of the 2D nanocrystal as Fig. 1.

Electron Diffraction Analysis

Experimental evidence for variations in stacking sequence in chemically exfoliated *h*-BN nanosheets also comes from an analysis of electron diffraction patterns. The ratio of the intensities in the electron diffraction pattern is related to the corresponding squared modulus ratio of the structure factors

$$\frac{I_{hki\ell}}{I_{h'k'i'l'}} \approx \frac{|F_{hki\ell}|^2}{|F_{h'k'i'l'}|^2} \quad \text{S.1}$$

where $(hki\ell)$ and $(h'k'i'l')$ are the Miller-Bravais indices of the diffraction planes.

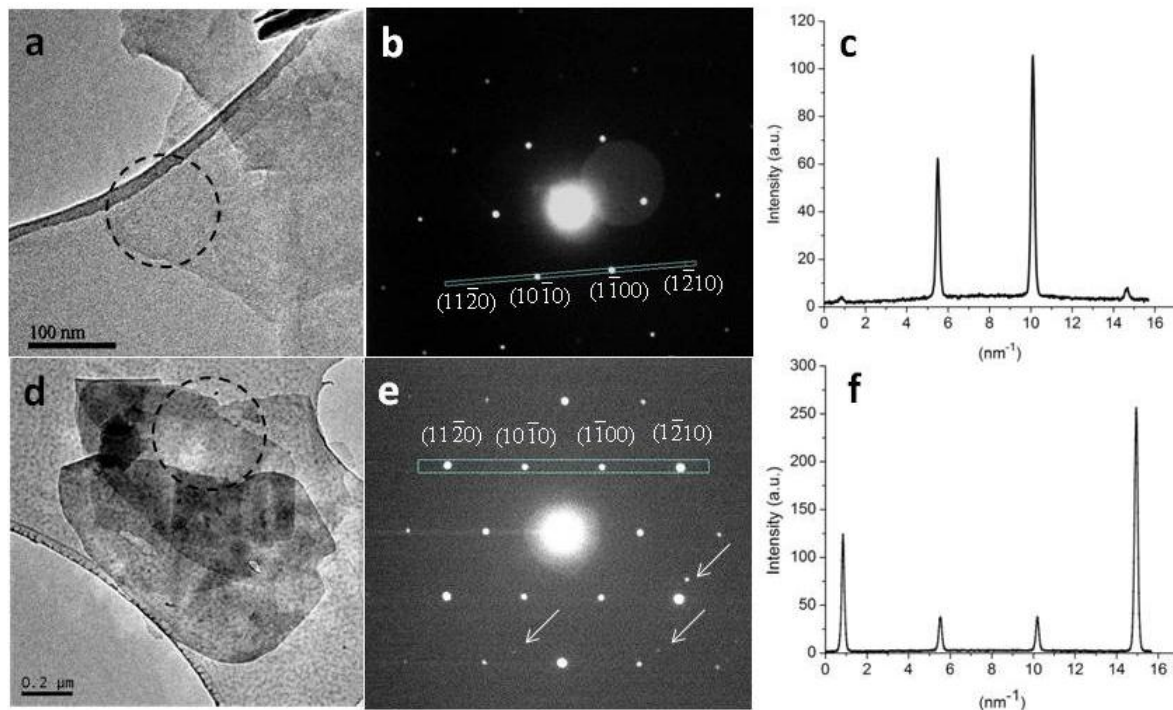


Figure S2.1: Low magnification TEM images with corresponding (b) and (e) SAED patterns and (c) and (f) measured intensity profiles as marked. Additional spots marked with arrows in (e) are likely to correspond to the presence of in-plane rotated layers.

In the typical low resolution TEM images of *h*-BN nanosheets with selected area electron diffraction (SAED) patterns and intensity profiles (Fig. S2.1), the intensities of the $\{10\bar{1}0\}$

reflections, $I_{\{10\bar{1}0\}}$, appear higher than those for the $\{11\bar{2}0\}$ reflections, $I_{\{11\bar{2}0\}}$, with a ratio

$I_{\{10\bar{1}0\}}/I_{\{11\bar{2}0\}} = 9.3 \pm 2.5$ (Fig. S2.1b). This experimental value is much higher than any of the

calculated ones (Table S1) with the nearest calculated being 1.1 corresponding to simple AA' or AA stackings. Possible explanations for the much larger experimental intensity ratios are crystal tilt, excitation error, or Debye-Waller attenuation of the higher order spatial frequencies. Fig. S2.1e shows the opposite where $I_{\{10\bar{1}0\}} < I_{\{11\bar{2}0\}}$ and $I_{\{10\bar{1}0\}}/I_{\{11\bar{2}0\}} = 0.29 \pm 0.09$. This is

remarkably close to the one calculated for Bernal AB stacking. However, this calculated ratio is not obtained exclusively for AB stacking and similar values can be obtained for a combination of AA' and ABC stacking sequences. For this reason SAED analysis cannot be used as a fully quantitative tool for the determination of stacking sequences in *h*-BN. However, it can nevertheless be used to support data from other techniques to confirm that stacking variations from the common AA' sequence can indeed exist within 2D *h*-BN nanostructures.

Table S1: Calculated ratio, $I_{\{10\bar{1}0\}}/I_{\{11\bar{2}0\}}$, for the stacking sequences described in Scheme 1.

	Ratio ($I_{\{10\bar{1}0\}}/I_{\{11\bar{2}0\}}$)					
No. of layers:	1	2	3	5	11	bulk
AA', AA	1.1	1.1	1.1	1.1	1.1	1.1
AB	1.1	0.28	0.37	0.31	0.28	0.28
ABC	1.1	0.28	0	0.04	0.01	0

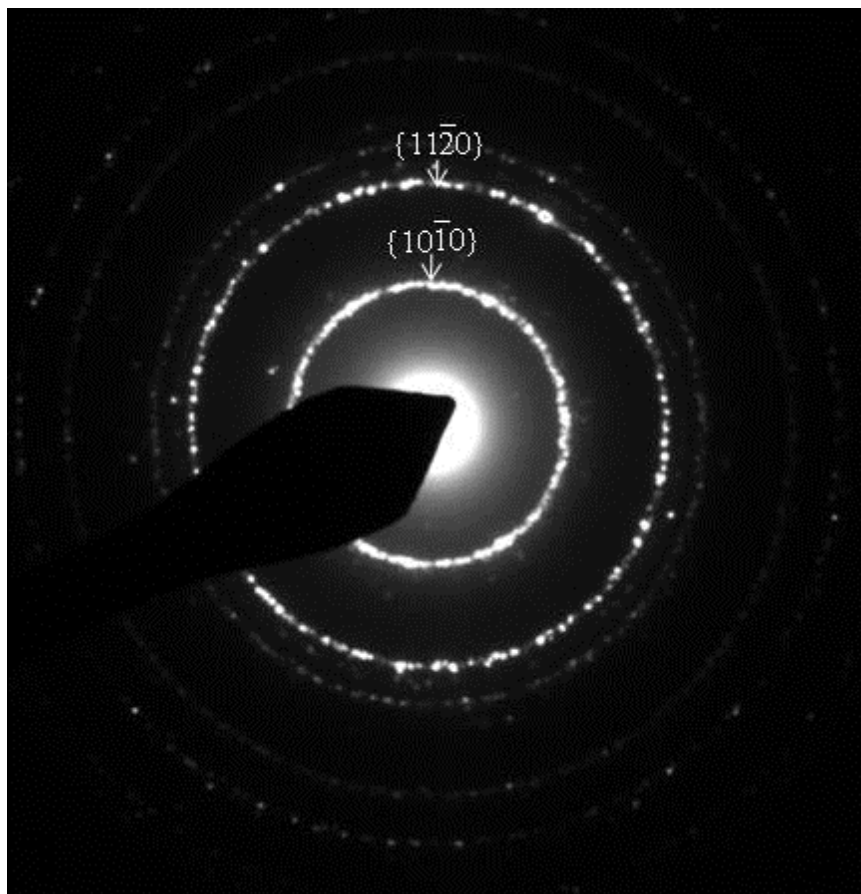


Figure S2.2: Electron diffraction pattern of the *h*-BN nanofilm.

Fig. S2.2 shows typical diffraction pattern of the *h*-BN nanofilm. In order to assess the stacking the ratio, $I_{\{10\bar{1}0\}}/I_{\{11\bar{2}0\}}$, was calculated. $I_{\{10\bar{1}0\}}$ and $I_{\{11\bar{2}0\}}$ values were obtained by integrating intensities along the circular regions of the diffraction pattern and corrected for the background. In order to account for parts of the diffraction pattern blocked by the beam stopper the angular limits of integration were from 0 to π .

Strain Measurements

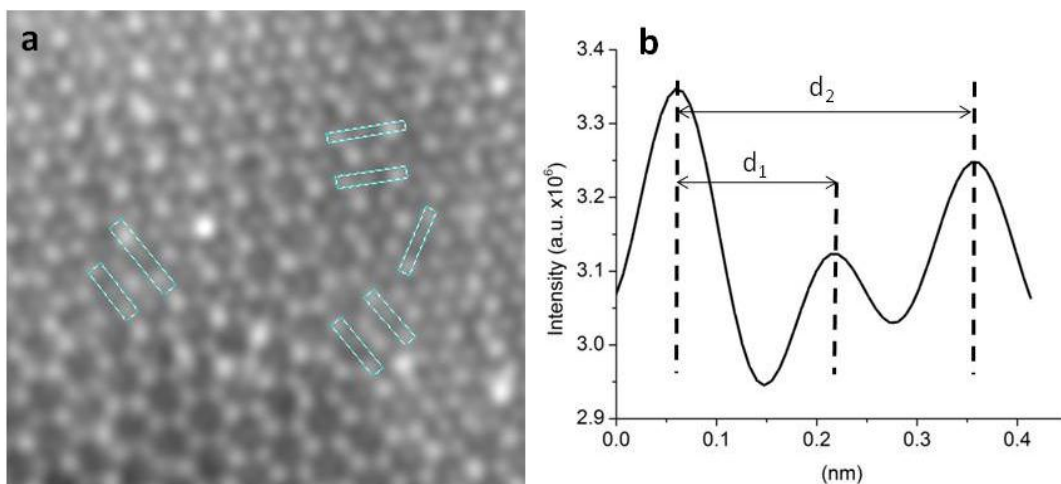


Figure S3: (a) Sub-region taken from the image in Fig. 2a with indications of the positions for shear strain measurements. (b) Example of the intensity profile from the Fig. S3a.

Table 2: Distance values d_1 and d_2 defined in Fig. S4b; and shear strain values. Indications of the positions for shear strain measurement are shown in Fig. S3a.

d_1 (nm)	0.12	0.17	0.13	0.13	0.18	0.11	0.12
d_2 (nm)	0.32	0.29	0.30	0.29	0.30	0.28	0.29
Shear Strain (%)	12	6.5	5.5	4.4	8.6	8.7	7.5

Shear strain was calculated according to the formula:

$$\text{Shear strain} = \frac{|0.5d_2 - d_1|}{0.5c} \times 100\% \quad \text{S.2}$$

where $0.5c = 0.33 \text{ nm}$ is interlayer distance in the *h*-BN (AA').

Effect of non-round aberrations

One possibility is that the intensity difference between nearest neighbour sites observed in Fig. 2c and interpreted as the novel AA stacking can be effect of higher order non-round aberrations. Here, we investigated whether three-fold astigmatism, A_2 , can produce such asymmetry in the bilayer *h*-BN (AA' stacking). The rotational alignment of the A_2 with respect to the lattice is defined relative to the N-B bond direction (Fig. S4.1a). It must be noted that due to its three-fold symmetry, A_2 does not influence the relative intensity of the nearest neighbour sites when it has direction 0° , 60° , 120° etc... Therefore, it should be sufficient to consider several angle-values of A_2 between 0° and 30° .

We investigated following directions of A_2 : 0° , 11° , 15° , 30° . The reason for choosing 11 degrees direction shall become clear later in this paragraph. $A_2 = 50 \text{ nm}$ was selected as a typical residual value for a well-corrected microscope¹.

One of the simulated images is shown in Fig. S4.1a. It is difficult to visually assess the asymmetry of the nearest neighbour sites, therefore the corresponding intensity profiles (dot-marked in Fig. S4.1a) are for easiness shown in Fig. S4.1b.

11°, 15°, and 30° directions produce noticeable difference in intensities while 0° has no effect, as expected. According to this very first analysis there are chances that the asymmetries noticed in Fig. 2c are indeed related to the presence of residual A_2 . The magnitude of the effect is approximately the same as displayed in experimental image (Fig. S4.3c).

However, if A_2 is responsible for these asymmetries, it must have similar effect on other images acquired immediately before or after, during the same microscope session. The bilayer and thicker regions of Fig. 1a do not demonstrate such effect. This means that A_2 is either negligible or is aligned along one of the following directions: 0°, 60°, 120°, etc. To disprove the latter point we have considered the hypothetical case of having a considerably high A_2 (> 50 nm) aligned along the 0° direction.

If we consider the relative orientation of the lattices displayed in Figs. 1a and 2c (reproduced in Figs. S4.2 and S4.3 for easiness together with the corresponding Fast Fourier Transforms, FFTs) we notice that these lattices are rotated 30° off each other. Accidentally, as demonstrated by the simulations reported in Fig. S4.1b, A_2 does indeed have an effect at 30°. Therefore we acknowledge that this particular case could be misleading and indeed due to residual non-round aberrations along the 30° direction rather than to a non-bulk stacking arrangement. However, if this is the case, similar effects would have to be noticed also in other images recorded immediately before or after, during the same session.

To avoid misinterpretations, the effect of possible residual A_2 should instead be better accounted for lattice rotations ranging between 11° and 30°. Fig. S4.4 in particular shows a nanoflake which does not have intensity difference between nearest neighbour sites and is rotated at 11° relatively to the original nanoflake in Fig. 1a. This case proves that A_2 is negligible and that our experimental asymmetries are indeed due to non-bulk stacking.

Furthermore, it should also be noted that the influence of the A_2 in the simulated results in Fig. S4.1 is overestimated: other residual non-round aberrations are expected to partially offset and cancel-out asymmetries introduced by A_2 .

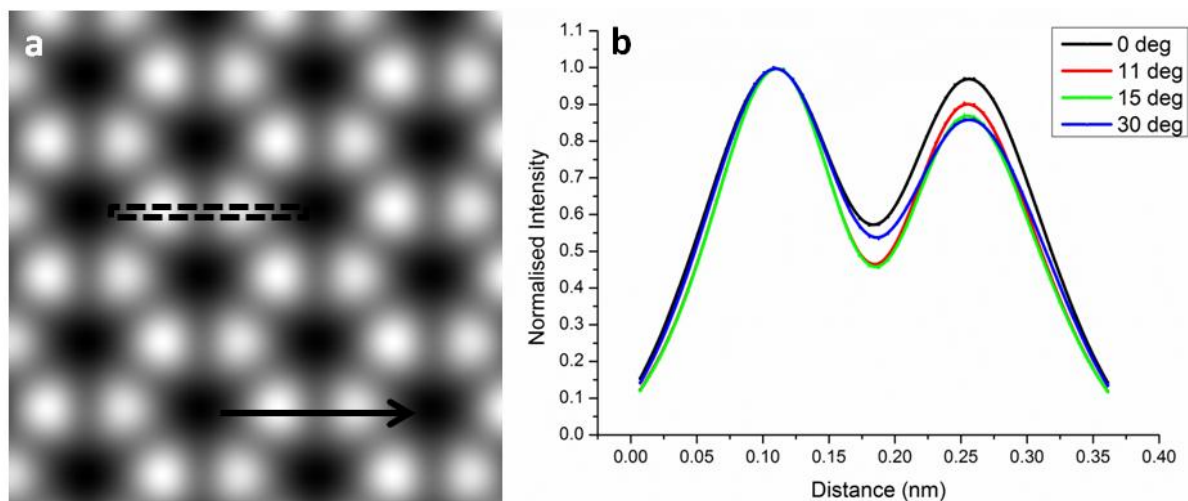


Figure S4.1. (a) Simulated image of the *h*-BN bilayer. (b) Intensity profiles across nearest neighbour columns (as indicated in part (a)) for the simulated images with $A_2 = 50$ nm for the different orientations. The arrow in part (a) indicates direction relative to which A_2 is aligned. Simulations were carried out using E. J. Kirkland code².

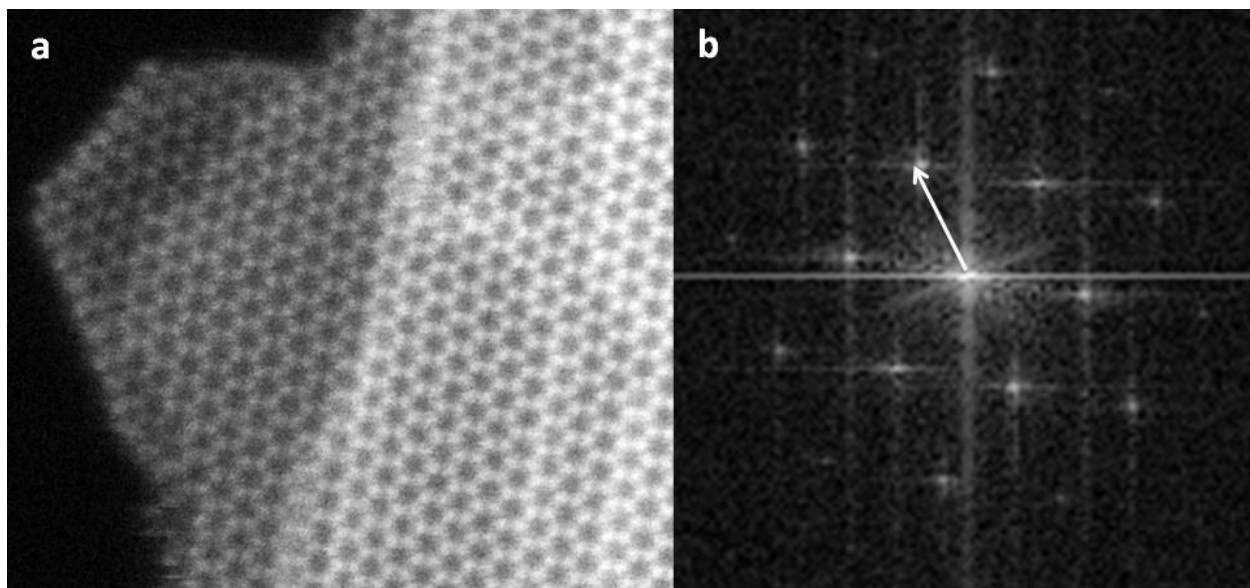


Figure S4.1. (a) Reproduction of Fig. 1(a) with (b) corresponding FFT. The arrow is drawn for easy visualisation of the lattice orientation.

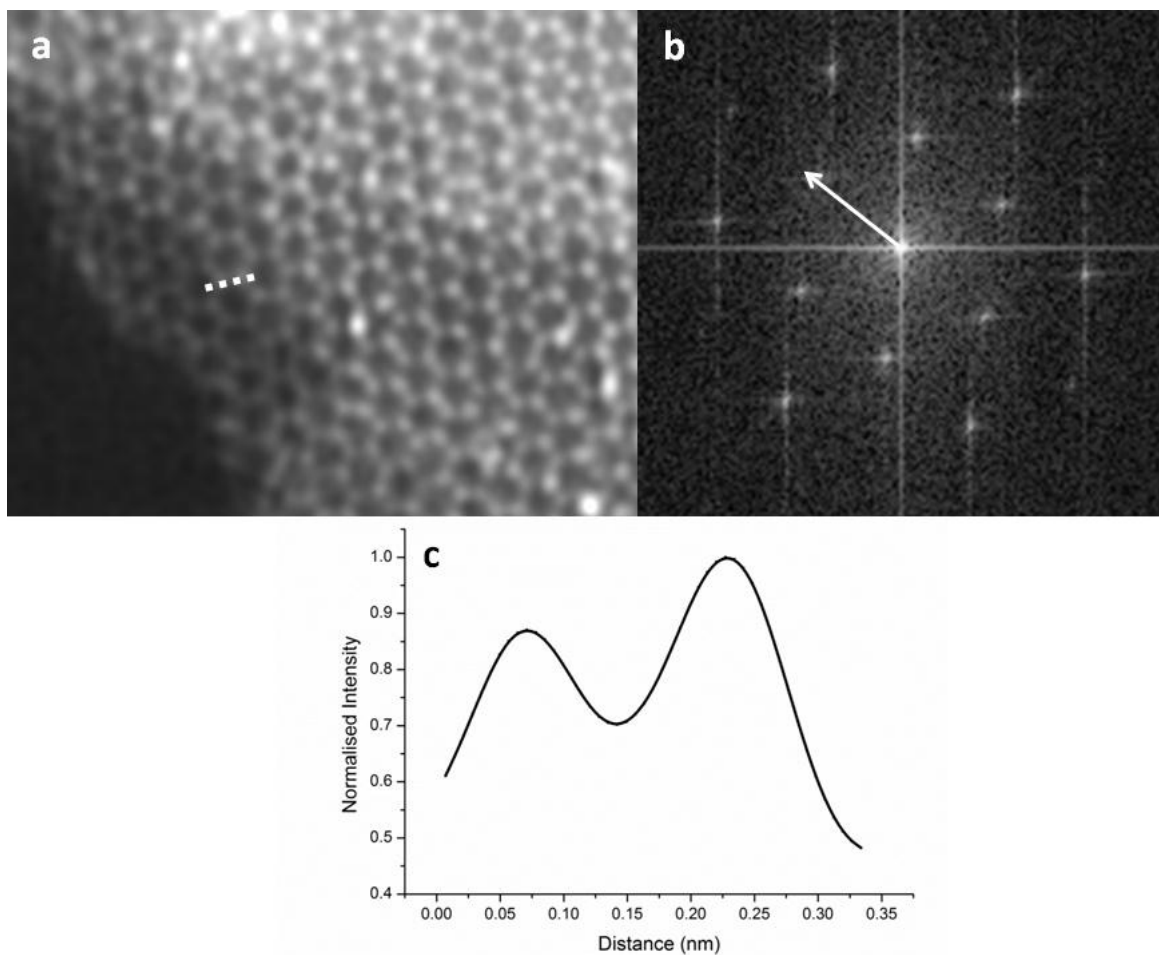


Figure S4.3. (a) Reproduction of Fig. 2(c) with (b) corresponding FFT. The arrow is drawn for easy visualisation of the lattice orientation. (c) Intensity profile corresponding to the dotted line in part (a).

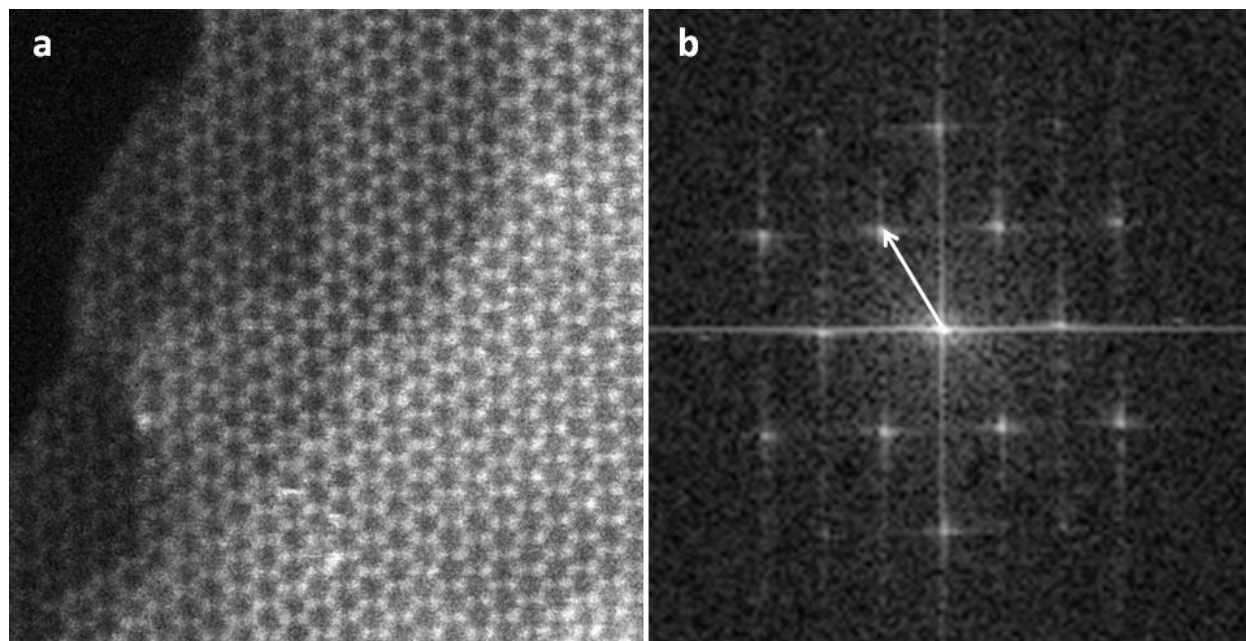


Figure S4.4. (a) ADF STEM image of *h*-BN nanoflake with (b) corresponding FFT.

Assessment of the impurities' atomic number

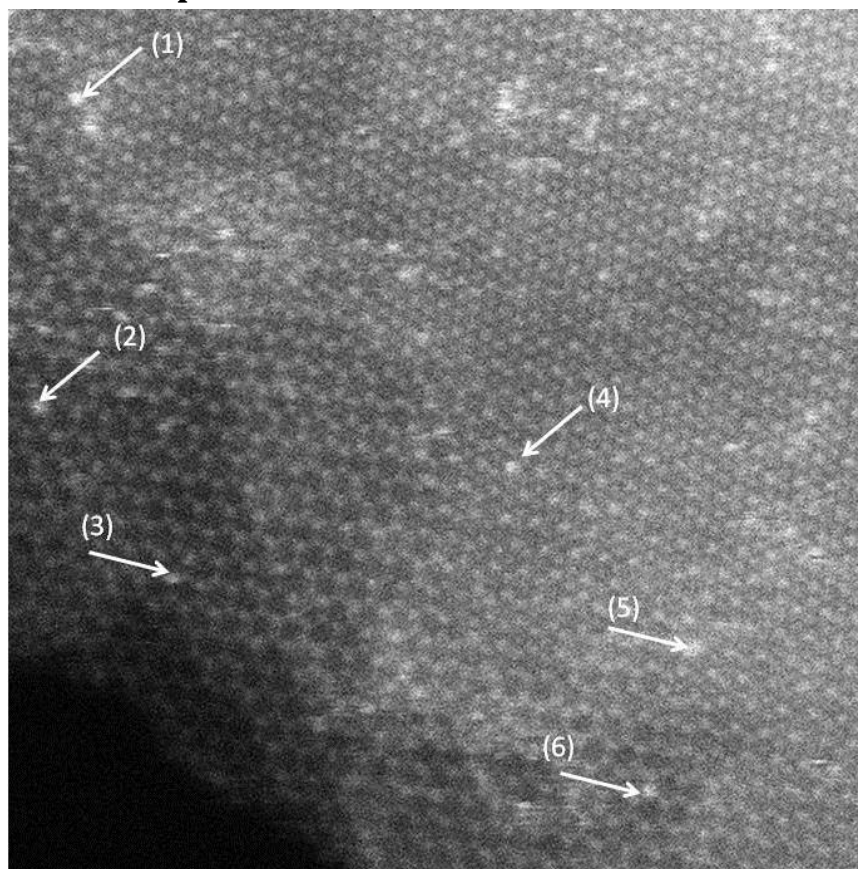


Figure S5: Unprocessed version of the image in Fig. 2a. Arrows indicate atomic columns containing impurity atoms.

Table S3: Intensity at atomic columns containing impurities (I_{imp}); intensity of equivalent sites not containing impurities (I_{equiv}) and the difference between the two I_{diff} ; the number of layers in equivalent sites (n); and the atomic number corresponding to the impurities (Z_{imp}). The impurity positions used are indicated in Fig. S5.

Impurity No.	1	2	3	4	5	6
I_{imp}	1.04	0.6	0.45	0.8	0.85	0.71
I_{equiv}	0.555	0.36	0.28	0.55	0.68	0.44
I_{diff}	0.485	0.24	0.17	0.25	0.17	0.27
n	5	3	3	5	5	4
Z_{imp}	14	9	8	10	7	10

The atomic number of the impurities was calculated as:

$$\frac{I_{\text{diff}}}{I_{\text{equiv}}} = \frac{1}{n} \left(\frac{Z_{\text{imp}}}{Z_{\text{BN}}} \right)^{1.7}$$

S.3

where $Z_{\text{BN}} = 6$ is the mean atomic number of the *h*-BN.

It must be stressed that this is approximate calculation of the atomic number of the impurities. Moreover, multislice calculations suggest that atomic number of the impurity cannot be estimated precisely without knowledge whether impurity is substitutional or an ad-atom.

Quantum chemical calculations

In order to facilitate the analysis of the experimental data and to understand how the stacking sequences in bi-layer *h*-BN can change in the presence/addition of impurity atoms we have performed theoretical quantum chemical calculations. For this purpose we used the Gaussian 03 software³, varying stacking sequences in *h*-BN bilayer sheets, using a model of two flakes with 54 and 24 atoms located symmetrically one on top of the other and registered along [001]. Structure optimisations of all models were performed using the Hartree-Fock method with the split valence 6-31G* polarized basis set^{4,5}. Models were also optimised after placing three Na⁺ ions at the edges of the bi-layer models. The dissociation energies at zero K were then determined using the optimised geometries as the difference between the sum of energies of two separate flakes and three separate sodium ions and the associated bilayer models. Single point energies of the species optimised at the HF/6-31G* level were also computed at the second order of Møller-Plesset perturbation theory⁶, MP2/6-31G*, and the dissociation energies were calculated to assess the influence of the electron correlation on the stability of the bilayer models. The results of the calculations are shown in Table S4. The optimised models are presented in Figure S6.

Table S4: Computed dissociation energies (kJ mol⁻¹) for the models with different stacking sequences stabilised by adsorbed Na⁺ ions.

Stacking Sequence	HF/6-31G*	HF/6-31G*//MP2/6-31G*
AA'	915.6	1079.5
AA	489.4	521.4

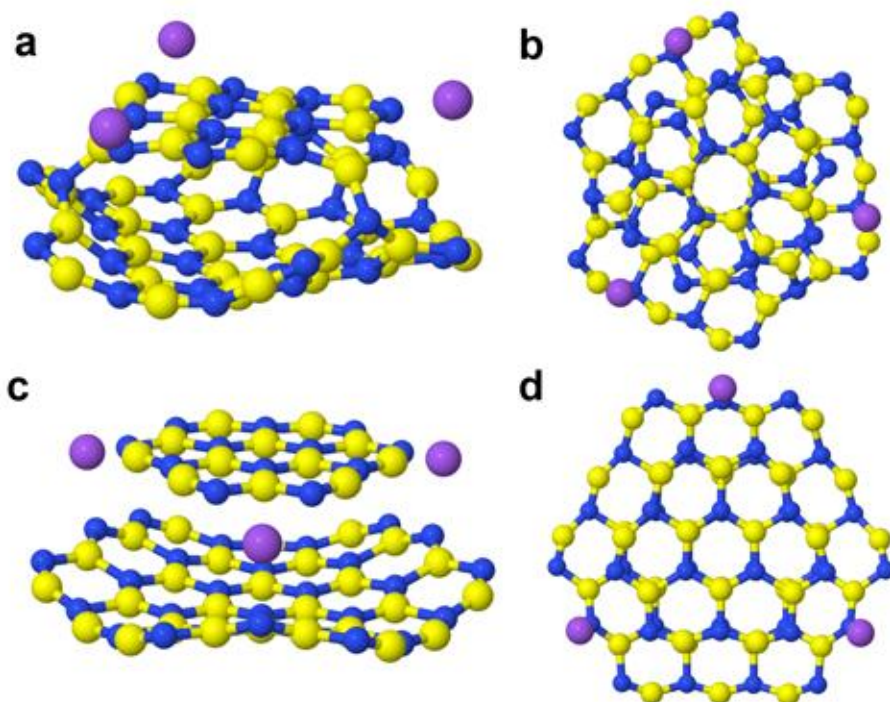


Figure S6: Energy-optimised models of the bilayer *h*-BN with adsorbed Na⁺ ions. A model with AA' stacking viewed along (a) [110] and (b) along [001] projections. A model with AA stacking viewed along (c) [110] and (d) along [001] projections. Nitrogen atoms are blue, boron atoms are yellow and sodium atoms are lilac.

Positive dissociation energies correspond to stabilisation of the associated structures. The considerably higher dissociation energy for the AA' model as compared to the AA model reflects formation of the B-N bonds between the two layers after the layers are rotated. The adsorbed Na⁺ ions cause the layers to rotate to maximize their interactions with the N atoms in the layers. The interaction energy between the single Na⁺ ion and the *h*-BN bilayer model can be estimated as approximately one third of the dissociation energy for the AA model.

SI References

- [1] Sawada, H.; Tomita, T.; Naruse, M.; Honda, T.; Hambridge, P.; Hartel, P.; Haider, M.; Hetherington, C.; Doole, R.; Kirkland, A.; Hutchison, J.; Titchmarsh, J.; Cockayne, D. *Journal of Electron Microscopy*, **54**, 119–21, (2005).
- [2] Kirkland, E. J. *Advanced Computing in Electron Microscopy*, 2nd ed. (2010)
- [3] Frisch, M. J et al. *Gaussian 03*. Gaussian Inc: Wallingford, CT. (2004).
- [4] Hehre, W.J. Self-consistent molecular orbital methods. XII. Further extensions of Gaussian-type basis sets for use in molecular orbital studies of organic molecules. *J. Chem. Phys.* **56**, 2257, (1972).
- [5] Hariharan, P. C. and Pople, J. A. The influence of polarization functions on molecular orbital hydrogenation energies. *Theo. Chim. Acta* **28**, 213-222, (1973).
- [6] Møller, C. and Plesset, M.S. *Phys. Rev.* **46**, 618-622, (1934).

